

A Compact Gas-Kinetic Scheme with Scalable Geometric Multigrid Acceleration for Steady-State Computation on 3D Unstructured Meshes

Hongyu Liu^{a,b}, Xing Ji^{a,*}, Yunpeng Mao^a, Yuan Ding^b, Kun Xu^{b,c,d}

^a*Shaanxi Key Laboratory of Environment and Control for Flight Vehicle, Xi'an Jiaotong University, Xi'an, China*

^b*Department of Mathematics, Hong Kong University of Science and Technology, Clear Water Bay, Kowloon, Hong Kong*

^c*Department of Mechanical and Aerospace Engineering, Hong Kong University of Science and Technology, Clear Water Bay, Kowloon, Hong Kong*

^d*Shenzhen Research Institute, Hong Kong University of Science and Technology, Shenzhen, China*

Abstract

In this paper, we present an advanced high-order compact gas-kinetic scheme (CGKS) for 3D unstructured mixed-element meshes, augmented with a geometric multigrid technique to accelerate steady-state convergence. The scheme evolves cell-averaged flow variables and their gradients on the original mesh. Mesh coarsening employs a two-step parallel agglomeration algorithm using a random hash for cell interface selection and a geometric skewness metric for deletion confirmation, ensuring both efficiency and robustness. For the coarser meshes, first-order kinetic flux vector splitting (KFVS) schemes with explicit or implicit time-stepping are used. The proposed multigrid CGKS is tested across various flow regimes on hybrid unstructured meshes, demonstrating significant improvements. A three-layer V-cycle multigrid strategy, coupled with an explicit forward Euler method on coarser levels, results in a convergence rate up to ten times faster than standard CGKS. In contrast, the implicit lower-upper symmetric Gauss-Seidel (LU-SGS) method offers limited convergence acceleration. Our findings indicate that the explicit multigrid CGKS is highly scalable and effective for large-scale computations, marking a substantial step forward in computational fluid dynamics.

Keywords: compact gas-kinetic scheme, geometric multigrid, unstructured mesh

1. Introduction

In the past few decades, the high-order numerical methods in computational fluid dynamics (CFD) have achieved great success [17, 1]. These methods, such as Weighted Essentially

*Corresponding author

Email addresses: hliudv@connect.ust.hk (Hongyu Liu), xjiad@connect.ust.hk (Xing Ji), m691810014@stu.xjtu.edu.cn (Yunpeng Mao), 1219948011@qq.com (Yuan Ding), makxu@ust.hk (Kun Xu)

Non-Oscillatory (WENO) [15], Discontinuous Galerkin (DG) [40, 41], Correction Procedure Via Reconstruction (CPR) [16, 47], and Variational Finite Volume (VFFV) [9], have played a crucial role in improving the accuracy of numerical simulations [6]. They are well-suited for handling complex flow phenomena, including turbulent flows [28], shock propagation [36], and multi-physics coupling [14].

In recent years, the high-order compact gas-kinetic scheme (CGKS) [19, 58, 56] has developed based on gas-kinetic theory. CGKS uses the time-dependent distribution function which has an accurate analytical integral solution at the cell interface of the Bhatnagar–Gross–Krook equation [5]. By using the accurate time-dependent distribution function at the cell interface, not only the Navier-Stokes flux functions can be obtained, but also the time accurate macroscopic flow variables will be evaluated. It means while cell-averaged flow variables are being updated under the finite volume framework, the cell-averaged gradients can also be updated by the Gauss-Green theorem. With the cell-averaged flow variables and their gradients, a Hermite Weighted Essentially Non-Oscillatory (HWENO) [26] method can be employed for the reconstruction, which can be found in our previous work of third-order CGKS [55]. As for temporal discretization, explicit two-stage fourth-order and other multi-stage multi-derivative time marching schemes can be used in CGKS for high-order temporal discretization [27]. Due to the benefits of the more reliable evolution process based on mesoscopic gas kinetic theory, the CGKS has excellent performance on both smooth and discontinuous flow regimes. The CGKS also shows good performance in the regime of unsteady compressible flow, such as in computational aeroacoustics [57] and implicit large eddy simulation [22]. In CGKS, the compression factor extends beyond the assumptions of the finite volume framework by determining the presence of discontinuities within the cell for the upcoming time step. Thus, it further improves the robustness of the CGKS when facing strong discontinuity. As a result, CGKS also performs well in supersonic and hypersonic flow simulations on the three-dimensional hybrid unstructured mesh, such as YF-17 fighter jet and X-38 type spaceship [20]. In summary, the CGKS demonstrates strong grid adaptability and robustness, effectively handling the complexities of low-quality meshes and pronounced discontinuities.

However, for the practical engineering problems with large-scale simulations, the explicit time marching approach has strong time-step size limitation for steady-state flow simulation. To speed up the convergence, acceleration techniques need to be employed. There are two mainstream ways for steady state acceleration, implicit temporal discretization and multigrid strategy. On one side, the implicit method is usually based on the lower-upper symmetric Gauss-Seidel (LU-SGS) method [2] or the Generalized minimal residual (GMRES) method [51, 38, 49]. Both methods above use the fully implicit temporal discretization to solve the linear system derived from the original equations through a linearization process. The implicit techniques have also been constructed for GKS and the unified gas kinetic scheme (UGKS) [43, 25, 60]. Due to the highly nonlinear evolution function of CGKS at the cell interface, it is nontrivial to get the approximate or even accurate Jacobian matrix for the cell-averaged gradients in the development of implicit CGKS. Because LU-SGS method has difficulties in dealing with the parallel boundary, it's difficult to apply the large-scale simulation method [45]. Compared with LU-SGS method, GMRES solves the linear system

more accurately and can have a faster convergence rate. More investigations have been done to improve the performance and portability of the GMRES algorithm for unstructured mesh in industrial CFD solvers [33]. However, due to the inherent sequential properties, GMRES encountered difficulties in achieving high parallel computing performance. Diverse HPC architecture trends also introduce challenges in algorithm migration of GMRES [53]. More importantly, preconditioners play a crucial role in influencing the stability and convergence rate of GMRES. Therefore, the selection of suitable preconditioners for GMRES in solving various compressible flow scenarios remains an unresolved and significant question. [35].

On the other hand, the geometric multigrid strategy has been developed for decades and is widely used in the second order schemes [8, 42, 48, 7]. Meanwhile, a series of p-multigrid methods have been developed for compact methods with multiple degrees of freedom in each cell [37, 30, 3, 29]. The equations are solved by different orders of accuracy in p-multigrid methods. Each order in p-multigrid is taken as a level of grid in geometric multigrid. The restriction and correct operators used in p-multigrid are the same as geometric-multigrid.

In this paper, an efficient and robust hybrid method of geometric-multigrid and p-multigrid for accelerating the CGKS in steady-state simulation is developed. On the finest level of mesh, the third-order explicit CGKS is employed to evolve both cell-averaged flow variables and cell-averaged gradients. Then the solution of flow variables and residuals are restricted to the coarse-level mesh. To guarantee the solution's accuracy, a force term will be constructed on the right-hand side of the equation. On the coarse levels of mesh, the first-order explicit kinetic flux vector splitting (KFVS) scheme is used only to update the cell-averaged flow variables. Then the solution will be prolonged back to the finest level. In this paper, a three-layer geometric multigrid is used. Benefiting from the explicit time marching scheme, geometric multigrid CGKS has the advantage of having consistent results between serial and parallel computations. Moreover, the local time-stepping strategy is very easy to apply in the geometric multigrid CGKS. As a result, it is convenient to apply geometric multigrid CGKS to large-scale computations. The computational cost between the explicit and geometric multigrid iteration is compared through the computations for nearly incompressible and supersonic flows under three-dimensional hybrid unstructured meshes, and the results indicate the algorithm this paper developed has a good convergence rate and grid adaptability.

The paper is organized as follows. In Section 2, the basic BGK equation, the finite volume framework and the construction method of GKS on three-dimensional hybrid unstructured mesh will be introduced. In Section 3, the third-order nonlinear spatial reconstruction and limiting procedure will be introduced. In Section 4, the mesh coarsening method and the strategy of the geometric multigrid method will be introduced. In Section 5, numerical examples including both inviscid and viscous flow computations will be given. The last section is conclusion.

2. High order compact gas kinetic scheme framework

2.1. 3-D BGK equation

The Boltzmann equation [10] describes the evolution of molecules at the mesoscopic scale. It indicates that each particle will either transport with a constant velocity or encounter a two-body collision. The BGK [5] model simplifies the Boltzmann equation by replacing the full collision term with a relaxation model. The 3-D gas-kinetic BGK equation [5] is

$$f_t + \mathbf{u} \cdot \nabla f = \frac{g - f}{\tau}, \quad (1)$$

where $f = f(\mathbf{x}, t, \mathbf{u}, \xi)$ is the gas distribution function, which is a function of space \mathbf{x} , time t , phase space velocity \mathbf{u} , and internal variable ξ . g is the equilibrium state and τ is the collision time, which means an averaged time interval between two sequential collisions. g is expressed as a Maxwellian distribution function. Meanwhile, the collision term on the right-hand side (RHS) of Eq. (1) should satisfy the compatibility condition

$$\int \frac{g - f}{\tau} \boldsymbol{\psi} d\Xi = 0,$$

where $\boldsymbol{\psi} = (1, \mathbf{u}, \frac{1}{2}(\mathbf{u}^2 + \xi^2))^T$, $d\Xi = du_1 du_2 du_3 d\xi_1 \dots d\xi_K$, K is the number of internal degrees of freedom, i.e. $K = (5 - 3\gamma)/(\gamma - 1)$ in the 3-D case, and γ is the specific heat ratio. The details of the BGK equation can be found in [50].

In the continuous flow regime, distribution function f can be taken as a small-scale expansion of Maxwellian distribution. Based on the Chapman-Enskog expansion [11], the gas distribution function can be expressed as [50],

$$f = g - \tau D_{\mathbf{u}} g + \tau D_{\mathbf{u}} (\tau D_{\mathbf{u}}) g - \tau D_{\mathbf{u}} [\tau D_{\mathbf{u}} (\tau D_{\mathbf{u}}) g] + \dots,$$

where $D_{\mathbf{u}} = \partial/\partial t + \mathbf{u} \cdot \nabla$. Through zeroth-order truncation $f = g$, the Euler equation can be obtained. The Navier-Stokes (NS) equations,

$$\mathbf{W}_t + \nabla \cdot \mathbf{F}(\mathbf{W}, \nabla \mathbf{W}) = 0,$$

can be obtained by taking first-order truncation, i.e.,

$$f = g - \tau(\mathbf{u} \cdot \nabla g + g_t), \quad (2)$$

with $\tau = \mu/p$ and $Pr = 1$.

Benefiting from the time-accurate gas distribution function, a time evolution solution at the cell interface is provided by the gas kinetic solver, which is distinguishable from the Riemann solver with a constant solution. This is a crucial point to construct the compact

high-order gas kinetic scheme.

$$\mathbf{W}(\mathbf{x}, t) = \int \boldsymbol{\psi} f(\mathbf{x}, t, \mathbf{u}, \xi) d\Xi, \quad (3)$$

and the flux at the cell interface can also be obtained

$$\mathbf{F}(\mathbf{x}, t) = \int \mathbf{u} \boldsymbol{\psi} f(\mathbf{x}, t, \mathbf{u}, \xi) d\Xi. \quad (4)$$

2.2. Finite volume framework

The boundary of a three-dimensional arbitrary polyhedral cell Ω_i can be expressed as

$$\partial\Omega_i = \bigcup_{p=1}^{N_f} \Gamma_{ip},$$

where N_f is the number of cell interfaces for cell Ω_i . $N_f = 4$ for tetrahedron, $N_f = 5$ for prism and pyramid, $N_f = 6$ for hexahedron. The semi-discretized form of the finite volume method for conservation laws can be written as

$$\frac{d\mathbf{W}_i}{dt} = \mathcal{L}(\mathbf{W}_i) = -\frac{1}{|\Omega_i|} \sum_{p=1}^{N_f} \int_{\Gamma_{ip}} \mathbf{F}(\mathbf{W}(\mathbf{x}, t)) \cdot \mathbf{n}_p ds, \quad (5)$$

with

$$\mathbf{F}(\mathbf{W}(\mathbf{x}, t)) \cdot \mathbf{n}_p = \int \boldsymbol{\psi} f(\mathbf{x}, t, \mathbf{u}, \xi) \mathbf{u} \cdot \mathbf{n}_p d\Xi,$$

where \mathbf{W}_i is the cell averaged values over cell Ω_i , $|\Omega_i|$ is the volume of Ω_i , \mathbf{F} is the interface fluxes, and $\mathbf{n}_p = (n_1, n_2, n_3)^T$ is the unit vector representing the outer normal direction of Γ_{ip} . Through the iso-parametric transformation, the Gaussian quadrature points can be determined and $\mathbf{F}_{ip}(t)$ can be approximated by the numerical quadrature

$$\int_{\Gamma_{ip}} \mathbf{F}(\mathbf{W}(\mathbf{x}, t)) \cdot \mathbf{n}_p ds = S_{i,p} \sum_{k=1}^M \omega_k \mathbf{F}(\mathbf{x}_{p,k}, t) \cdot \mathbf{n}_p,$$

where $S_{i,p}$ is the area of Γ_{ip} . Through the iso-parametric transformation, in the current study the linear element is considered. To meet the requirement of a third-order spatial accuracy, three Gaussian points are used for a triangular face and four Gaussian points are used for a quadrilateral face. In the computation, the fluxes are obtained under the local coordinates. The details can be found in [20, 34, 24].

2.3. Gas kinetic solver

In order to obtain the numerical flux at the cell interface, the integration solution based on the BGK equation is used

$$f(\mathbf{x}, t, \mathbf{u}, \xi) = \frac{1}{\tau} \int_0^t g(\mathbf{x}', t', \mathbf{u}, \xi) e^{-(t-t')/\tau} dt' + e^{-t/\tau} f_0(\mathbf{x} - \mathbf{u}t, \mathbf{u}, \xi), \quad (6)$$

where $\mathbf{x} = \mathbf{x}' + \mathbf{u}(t - t')$ is the particle trajectory. f_0 is the initial gas distribution function, g is the corresponding equilibrium state in the local space and time. This integration solution describes the physical picture of the particle evolution. Starting with an initial state f_0 , the particle will take free transport with a probability of $e^{-\Delta t/\tau}$. Otherwise, it will suffer a series of collisions. The effect of collisions is driving the system to the local Maxwellian distribution g , and the particles from the equilibrium propagate along the characteristics with a surviving probability of $e^{-(t-t')/\tau}$. The components of the numerical fluxes at the cell interface can be categorized as the upwinding free transport from f_0 and the central difference from the integration of the equilibrium distribution.

In order to construct a time-evolving gas distribution function at a cell interface, the following notations are introduced first

$$a_{x_i} \equiv (\partial g / \partial x_i) / g = g_{x_i} / g, \quad A \equiv (\partial g / \partial t) / g = g_t / g,$$

where g is the equilibrium state. The partial derivatives a_{x_i} and A , denoted by s , have the form of

$$s = s_j \psi_j = s_1 + s_2 u_1 + s_3 u_2 + s_4 u_3 + s_5 \frac{1}{2} (u_1^2 + u_2^2 + u_3^2 + \xi^2).$$

The initial gas distribution function in Eq. (6) can be modeled as

$$f_0 = f_0^l(\mathbf{x}, \mathbf{u}) \mathbb{H}(x_1) + f_0^r(\mathbf{x}, \mathbf{u}) (1 - \mathbb{H}(x_1)),$$

where $\mathbb{H}(x_1)$ is the Heaviside function. Here f_0^l and f_0^r are the initial gas distribution functions on the left and right sides of a cell interface, which can be fully determined by the initially reconstructed macroscopic variables. The first-order Taylor expansion for the gas distribution function in space around $\mathbf{x} = \mathbf{0}$ can be expressed as

$$f_0^k(\mathbf{x}) = f_G^k(\mathbf{0}) + \frac{\partial f_G^k}{\partial x_i}(\mathbf{0}) x_i = f_G^k(\mathbf{0}) + \frac{\partial f_G^k}{\partial x_1}(\mathbf{0}) x_1 + \frac{\partial f_G^k}{\partial x_2}(\mathbf{0}) x_2 + \frac{\partial f_G^k}{\partial x_3}(\mathbf{0}) x_3, \quad (7)$$

for $k = l, r$. According to Eq. (2), f_G^k has the form

$$f_G^k(\mathbf{0}) = g^k(\mathbf{0}) - \tau (u_i g_{x_i}^k(\mathbf{0}) + g_t^k(\mathbf{0})), \quad (8)$$

where g^k is the equilibrium state with the form of a Maxwell distribution. g^k can be fully determined from the reconstructed macroscopic variables $\mathbf{W}^l, \mathbf{W}^r$ at the left and right sides

of a cell interface

$$\int \boldsymbol{\psi} g^l d\Xi = \mathbf{W}^l, \int \boldsymbol{\psi} g^r d\Xi = \mathbf{W}^r. \quad (9)$$

Substituting Eq. (7) and Eq. (8) into Eq. (6), the kinetic part for the integral solution can be written as

$$e^{-t/\tau} f_0^k(-\mathbf{u}t, \mathbf{u}, \xi) = e^{-t/\tau} g^k [1 - \tau(a_{x_i}^k u_i + A^k) - t a_{x_i}^k u_i], \quad (10)$$

where the coefficients $a_{x_1}^k, \dots, A^k, k = l, r$ are defined according to the expansion of g^k . After determining the kinetic part f_0 , the equilibrium state g in the integral solution Eq. (6) can be expanded in space and time as follows

$$g(\mathbf{x}, t) = g^c(\mathbf{0}, 0) + \frac{\partial g^c}{\partial x_i}(\mathbf{0}, 0) x_i + \frac{\partial g^c}{\partial t}(\mathbf{0}, 0) t, \quad (11)$$

where g^c is the Maxwellian equilibrium state located at an interface. Similarly, \mathbf{W}^c are the macroscopic flow variables for the determination of the equilibrium state g^c

$$\int \boldsymbol{\psi} g^c d\Xi = \int_{u>0} \boldsymbol{\psi} g^l d\Xi + \int_{u<0} \boldsymbol{\psi} g^r d\Xi = \mathbf{W}^c. \quad (12)$$

Substituting Eq. (11) into Eq. (6), the collision part in the integral solution can be written as

$$\frac{1}{\tau} \int_0^t g(\mathbf{x}', t', \mathbf{u}, \xi) e^{-(t-t')/\tau} dt' = C_1 g^c + C_2 a_{x_i}^c u_i g^c + C_3 A^c g^c, \quad (13)$$

where the coefficients $a_{x_i}^c, A^c$ are defined from the expansion of the equilibrium state g^c . The coefficients $C_m, m = 1, 2, 3$ in Eq. (13) are given by

$$C_1 = 1 - e^{-t/\tau}, C_2 = (t + \tau) e^{-t/\tau} - \tau, C_3 = t - \tau + \tau e^{-t/\tau}.$$

The coefficients in Eq. (10) and Eq. (13) can be determined by the spatial derivatives of macroscopic flow variables and the compatibility condition as follows

$$\begin{aligned} \langle a_{x_1} \rangle &= \frac{\partial \mathbf{W}}{\partial x_1} = \mathbf{W}_{x_1}, \langle a_{x_2} \rangle = \frac{\partial \mathbf{W}}{\partial x_2} = \mathbf{W}_{x_2}, \langle a_{x_3} \rangle = \frac{\partial \mathbf{W}}{\partial x_3} = \mathbf{W}_{x_3}, \\ \langle A + a_{x_1} u_1 + a_{x_2} u_2 + a_{x_3} u_3 \rangle &= 0, \end{aligned} \quad (14)$$

where $\langle \dots \rangle$ are the moments of a gas distribution function defined by

$$\langle \langle \dots \rangle \rangle = \int \boldsymbol{\psi}(\dots) g d\Xi. \quad (15)$$

For the viscous flow, the physical relaxation time is determined by

$$\tau = \mu/p,$$

where μ is the dynamic viscosity coefficient and p is the pressure at the cell interface. In order to properly capture the unresolved shock structure, additional numerical dissipation is needed. The physical collision time τ in the exponential function part can be replaced by a numerical collision time τ_n ,

$$\tau_n = \frac{\mu}{p} + C \left| \frac{p_l - p_r}{p_l + p_r} \right| \Delta t,$$

where p_l and p_r denote the pressure on the left and right sides of the cell interface. The inclusion of the pressure jump term is to implement the non-equilibrium transport mechanism in the flux function to mimic the physical process in the shock layer. For the inviscid flow, the collision time τ_n is modified as

$$\tau_n = \varepsilon \Delta t + C \left| \frac{p_l - p_r}{p_l + p_r} \right| \Delta t,$$

where $\varepsilon = 0.01$ and $C = 1$. Then substitute Eq. (10) and Eq. (13) into Eq. (6) with τ and τ_n , the final second-order time-dependent gas distribution function becomes

$$\begin{aligned} f(\mathbf{0}, t, \mathbf{u}, \xi) = & (1 - e^{-t/\tau_n})g^c + [(t + \tau)e^{-t/\tau_n} - \tau]a_{x_i}^c u_i g^c + (t - \tau + \tau e^{-t/\tau_n})A^c g^c \\ & + e^{-t/\tau_n} g^l [1 - (\tau + t)a_{x_i}^l u_i - \tau A^l] H(u_1) \\ & + e^{-t/\tau_n} g^r [1 - (\tau + t)a_{x_i}^r u_i - \tau A^r] (1 - H(u_1)). \end{aligned} \quad (16)$$

2.4. Direct evolution of the cell averaged first-order spatial derivatives

As shown in Eq. (16), a time evolution solution at a cell interface is provided by the gas-kinetic solver, which is distinguished from the Riemann solvers with a constant solution. By recalling Eq. (3), the conservative variables at the Gaussian point $\mathbf{x}_{p,k}$ can be updated through the moments $\boldsymbol{\psi}$ of the gas distribution function,

$$\mathbf{W}_{p,k}(t^{n+1}) = \int \boldsymbol{\psi} f^n(\mathbf{x}_{p,k}, t^{n+1}, \mathbf{u}, \xi) d\Xi, \quad k = 1, \dots, M.$$

Then, the cell-averaged first-order derivatives within each element at t^{n+1} can be evaluated based on the divergence theorem,

$$\nabla \bar{W}^{n+1} |\Omega| = \int_{\Omega} \nabla \bar{W}(t^{n+1}) dV = \int_{\partial\Omega} \bar{W}(t^{n+1}) \mathbf{n} dS = \sum_{p=1}^{N_f} \sum_{k=1}^{M_p} \omega_{p,k} W_{p,k}^{n+1} \mathbf{n}_{p,k} \Delta S_p,$$

where $\mathbf{n}_{p,k} = ((n_1)_{p,k}, (n_2)_{p,k}, (n_3)_{p,k})$ is the outer unit normal direction at each Gaussian point $\mathbf{x}_{p,k}$.

3. Spatial reconstruction

The 3rd-order compact reconstruction [23] is adopted here with cell-averaged values and cell-averaged first-order spatial derivative. To maintain both shock-capturing ability and robustness, WENO weights and gradient compression factor (CF) are used [20]. Further improvement has been made to make reconstruction simple and more robust [55]. Only one large stencil and one sub-stencil are involved in the WENO procedure.

3.1. 3rd-order compact reconstruction for large stencil

Firstly, a linear reconstruction approach is presented. To achieve a third-order accuracy in space, a quadratic polynomial p^2 is constructed as follows

$$\begin{aligned} p^2 = & a_0 + a_1(x - x_0) + a_2(y - y_0) + a_3(z - z_0) \\ & + a_4(x - x_0)^2 + a_5(y - y_0)^2 + a_6(z - z_0)^2 \\ & + a_7(x - x_0)(y - y_0) + a_8(y - y_0)(z - z_0) + a_9(x - x_0)(z - z_0), \end{aligned}$$

The p^2 on Ω_0 is constructed on the compact stencil S including Ω_0 and all von Neumann neighbors Ω_m ($m = 1, \dots, N_f$, where $N_f = 6$ for hexahedron cell or $N_f = 5$ for triangular prism) of it. The cell averages \bar{Q} on Ω_0 and Ω_m together with cell averages of space partial derivatives \bar{Q}_x, \bar{Q}_y and \bar{Q}_z on Ω_m are used to obtain p^2 .

The polynomial p^2 is required to exactly satisfy cell averages over both Ω_0 and Ω_m ($m = 1, \dots, N_f$)

$$\iiint_{\Omega_0} p^2 dV = \bar{Q}_0 |\Omega_0|, \quad \iiint_{\Omega_m} p^2 dV = \bar{Q}_m |\Omega_m|,$$

with the following condition satisfied in a least-square sense

$$\begin{aligned} \iiint_{\Omega_m} \frac{\partial}{\partial x} p^2 dV &= (\bar{Q}_x)_m |\Omega_m| \\ \iiint_{\Omega_m} \frac{\partial}{\partial y} p^2 dV &= (\bar{Q}_y)_m |\Omega_m| \\ \iiint_{\Omega_m} \frac{\partial}{\partial z} p^2 dV &= (\bar{Q}_z)_m |\Omega_m|. \end{aligned}$$

To solve the above system, the constrained least-square method is used.

3.2. Green-Gauss reconstruction for the sub stencil

The classical Green-Gauss reconstruction [39] with only cell-averaged values is adopted to provide the linear polynomial p^1 for the sub stencil.

$$p^1 = \bar{Q} + \mathbf{x} \cdot \sum_{m=1}^{N_f} \frac{\bar{Q}_m + \bar{Q}_0}{2} S_m \mathbf{n}_m,$$

where S_m is the area of the cell's surface and \mathbf{n}_m is the surface's normal vector. In most cases, Green-Gaussian reconstruction has only first-order precision.

3.3. Gradient compression Factor

The CF was first proposed in [20]. Here several improvements have been made: there is no ϵ in the improved expression of CF; the difference of Mach number is added to improve the robustness under strong rarefaction waves. Denote $\alpha_i \in [0, 1]$ as gradient compression factor at targeted cell Ω_i

$$\alpha_i = \prod_{p=1}^m \prod_{k=0}^{M_p} \alpha_{p,k},$$

where $\alpha_{p,k}$ is the CF obtained by the k th Gaussian point at the interface p around cell Ω_i , which can be calculated by

$$\alpha_{p,k} = \frac{1}{1 + A^2},$$

$$A = \frac{|p^l - p^r|}{p^l} + \frac{|p^l - p^r|}{p^r} + (\text{Ma}_n^l - \text{Ma}_n^r)^2 + (\text{Ma}_t^l - \text{Ma}_t^r)^2,$$

where p is pressure, Ma_n and Ma_t are the Mach numbers defined by normal and tangential velocity, and superscripts l, r denote the left and right values of the Gaussian points.

Then, the updated slope is modified by

$$\widetilde{\nabla \mathbf{W}}_i^{n+1} = \alpha_i \overline{\nabla \mathbf{W}}_i^{n+1},$$

and the Green-Gauss reconstruction is modified as

$$p^1 = \overline{Q} + \alpha \mathbf{x} \cdot \sum_{m=1}^{N_f} \frac{\overline{Q}_m + \overline{Q}_0}{2} S_m \mathbf{n}_m.$$

3.4. Non-linear WENO weights

In order to deal with discontinuity, the idea of multi-resolution WENO reconstruction is adopted [20, 59]. Here only two polynomials are chosen

$$P_2 = \frac{1}{\gamma_2} p^2 - \frac{\gamma_1}{\gamma_2} p^1, P_1 = p^1.$$

where $\gamma_1 = \gamma_2 = 0.5$. So the quadratic polynomial p^2 can be written as

$$p^2 = \gamma_1 P_1 + \gamma_2 P_2. \tag{17}$$

Then, we can define the smoothness indicators

$$\beta_j = \sum_{|\alpha|=1}^{r_j} \Omega^{\frac{2}{3}|\alpha|-1} \iiint_{\Omega} (D^\alpha p^j(\mathbf{x}))^2 dV,$$

where α is a multi-index and D is the derivative operator, $r_1 = 1, r_2 = 2$. Special care is given for β_1 for better robustness

$$\beta_1 = \min(\beta_{1,\text{Green-Gauss}}, \beta_{1,\text{least-square}}),$$

where $\beta_{1,\text{Green-Gauss}}$ is the smoothness indicator defined by Green-Gauss reconstruction, and $\beta_{1,\text{least-square}}$ is the smoothness indicator defined by second-order least-square reconstruction. Then, the smoothness indicators β_i are non-dimensionalized by

$$\tilde{\beta}_i = \frac{\beta_i}{Q_0^2 + \beta_1 + 10^{-40}}.$$

The nondimensionalized global smoothness indicator $\tilde{\sigma}$ can be defined as

$$\tilde{\sigma} = \left| \tilde{\beta}_1 - \tilde{\beta}_0 \right|.$$

Therefore, the corresponding non-linear weights are given by

$$\tilde{\omega}_m = \gamma_m \left(1 + \left(\frac{\tilde{\sigma}}{\epsilon + \tilde{\beta}_m} \right)^2 \right), \epsilon = 10^{-5},$$

$$\bar{\omega}_m = \frac{\tilde{\omega}_m}{\sum \tilde{\omega}_m}, m = 1, 2.$$

Replacing γ_m in equation (17) by $\bar{\omega}_m$, the final non-linear reconstruction can be obtained

$$R(\mathbf{x}) = \bar{\omega}_2 P_2 + \bar{\omega}_1 P_1.$$

The desired non-equilibrium states at Gaussian points become

$$Q_{p,k}^{l,r} = R^{l,r}(\mathbf{x}_{p,k}), (Q_{x_i}^{l,r})_{p,k} = \frac{\partial R^{l,r}}{\partial x_i}(\mathbf{x}_{p,k}).$$

4. Mesh coarsening algorithm and geometric multigrid strategy

In this section, the geometric multigrid strategy is introduced. To construct the geometric multigrid strategy with nice process-level parallel computation performance, firstly, a mesh coarsening algorithm which can guarantee a fast enough speed of the coarse mesh generating is introduced. Then, the implementation of the geometric multigrid and p-multigrid CGKS is introduced. Finally, the parallel communication strategy of geometric multigrid CGKS is

introduced and the convergence histories under different conditions of parallel computation are shown to indicate the potential of the geometric multigrid CGKS in large-scale parallel computation.

4.1. Mesh coarsening algorithm

Since the number of cells in the large-scale simulation's mesh is usually very large, it is important to design an efficient algorithm for mesh coarsening. In this paper, a fast parallel mesh agglomeration algorithm is developed.

In this section, the face removal algorithm [54] is introduced first. To implement boundary conditions easily and transfer the information at the parallel interface efficiently, the boundary face and parallel interface will not be deleted. Considering a face with its left cell and right cell, its hash value is

$$h_f = [23(N_l + N_r) + N_l N_r] \% N_f \quad (18)$$

where h_f is the face's hash value, N_l is the index of the face's left cell, N_r is the index of the face's right cell, N_f is the total interior face number of the mesh. For example, if the face's left cell ID is 10, the face's right cell ID is 12, and the total face number of the mesh is 100, then the hash value of the face will be 5.

With the face's hash value calculation method, interior faces will be iterated and selected for the collection of faces to be deleted. When iterating at a face, the face's hash value will be calculated. Then, whether the hash value is already inserted in the built hash table will be determined. If the face's hash value has already been inserted in the hash table, the face will not be selected for the collection.

To guarantee coarse meshes' quality, the skewness factor will be introduced to indicate the quality of the mesh. When a face in the above collection is selected to be deleted, the virtual center of the cell which will be constructed by the face's left and right cells is

$$C_c = \frac{V_l C_l + V_r C_r}{V_l + V_r} \quad (19)$$

where V_l is the volume of the left cell, C_l is the center of the left cell, V_r is the volume of the right cell, and C_r is the center of the right cell. The angle between the unit normal vector of the face and the vector pointed from the virtual cell center to the face center is

$$\sin \alpha = \frac{d \cdot n}{|n|} \quad (20)$$

where α is the skewness angle representing the skewness factor, d is the distance vector pointed from the virtual cell center to the face center, and n is the face's unit normal vector shown in Fig. 1. If the angle is smaller than a value that has been set previously, which means the meshes' quality is bad, the face will not be deleted. To sum up, the cell merge algorithm can be summarized as Algorithm. 1 shows.

After coarsening the original mesh for the first time, the geometric variables of the coarse

Algorithm 1: Cell coarsening method

```

1 Initialization: the collection of faces to be deleted  $V_d$ , the collection's volume at
  begin is zero.;
2 for  $j=1,\dots,N_f$  do
3   Calculate the  $face_j$  's hash value by Eq. (18);
4   If the hash value hasn't appeared in the previous hash table, insert the face into
   the collection.
5 end
6 for  $i=1,\dots,N_i$  do
7   where  $N_i$  is the element in the collection of faces to be deleted;
8   Calculate the skewness of the face and its neighbor cells by Eq. (20);
9   If the skewness factor is bigger than the limit, then merge the left and right cells
   of the face;
10 end

```

cell should be recalculated. The volume of the coarse cell is

$$V_c = \sum_{i=0}^n V_i \quad (21)$$

where V_c is the volume of the coarse cell, V_i is the volume of the fine cell constructing the coarse cell. The center of the cell is

$$C_c = \frac{\sum_{i=0}^n V_i C_i}{V_c} \quad (22)$$

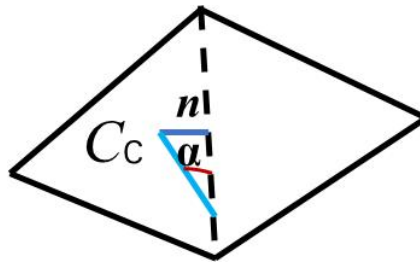


Figure 1: Skews angle factor .

4.2. Geometric multigrid and p-multigrid algorithm for third-order compact gas kinetic scheme

In this section, a hybrid method of geometric multigrid and p-multigrid method is employed in high-order compact gas kinetic scheme. For the finest mesh, the third-order gas kinetic scheme solver is used as the pre-smoother and post-smoother [31]. For the other

coarse meshes, the first-order KFVS solver is employed to be the pre-smoother and post-smoother. For the finest mesh, the semi-discretization equation can be written as

$$W_h^{n+1} = W_h^n + \frac{\delta V}{\delta t} \sum_j Res(W_h^n) \quad (23)$$

where W_h^{n+1} is the cell average conservative variable at step $n + 1$, W_h^n is the cell average conservative variable at step n , $Res(W_h^n)$ is the residual calculated at step n using cell average conservative variable W_h^n , h means fine level, and j means the j^{th} face of the current cell.

Having cell average value updated once means doing smooth once. After smoothing cell average value, residual used for restricting the coarse meshes residual can be updated by Eq. (23). Cell average conservative variable is restricted to coarse mesh by

$$W_{2h}^0 = \frac{\sum_{i \in cell_{2h}} V_{ifc} W_{ifc}}{V_{2h}} \quad (24)$$

where W_{2h}^0 is the initial conservative variable in the first step of coarse mesh calculation, V_{2h} is the coarse cell's volume, W_{ifc} is the i^{th} fine cell's conservative variable. Residual restricted from fine mesh to coarse mesh is guided by

$$Res_{2h}^* = \sum_{i \in cell_{2h}} Res_{ifc}^{n+1} \quad (25)$$

where Res_{2h}^* is the residual restricted from fine mesh, Res_{ifc}^{n+1} is the i^{th} fine cell's residual. It's important to notice that the physical meaning of the residual restriction process is the total flux of the coarse cell using the flux calculated from fine mesh. It is shown in Fig. 2.

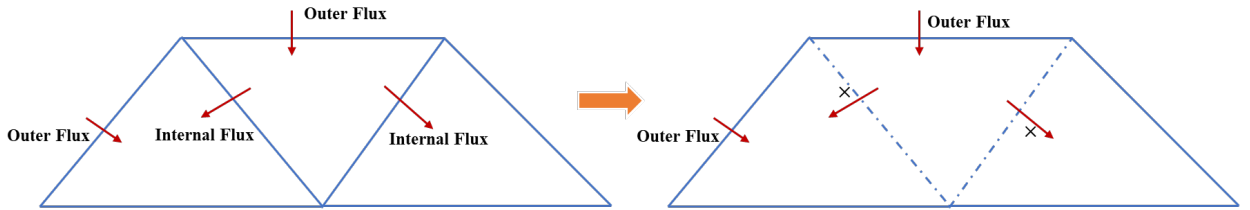


Figure 2: Physical picture of the flux relationship.

In order to guarantee the final result can still keep high order accuracy, a forcing term is given by

$$F = Res_{2h}^* - Res_{2h}(W_{2h}^0) \quad (26)$$

For the coarse mesh, the macroscopic variable is updated using forcing term by

$$W_{2h}^{k+1} = W_{2h}^k + \frac{\delta t}{\delta V} (Res_{2h}^k + F) \quad (27)$$

After updating the macroscopic variable on coarse mesh with some explicit steps, a correction process can be used to correct fine mesh solution by

$$W_h^* = W_h^{n+1} + (W_{2h}^{k+1} - W_{2h}^0) \quad (28)$$

It is important to note that the sum of the number of pre-smoothing and post-smoothing should not be less than 2. In this paper, without specified claiming the pre-smooth number is set to 1, and the post-smooth number is set to 0.

A three level V cycle geometric grid algorithm's picture is given by Fig. 3.

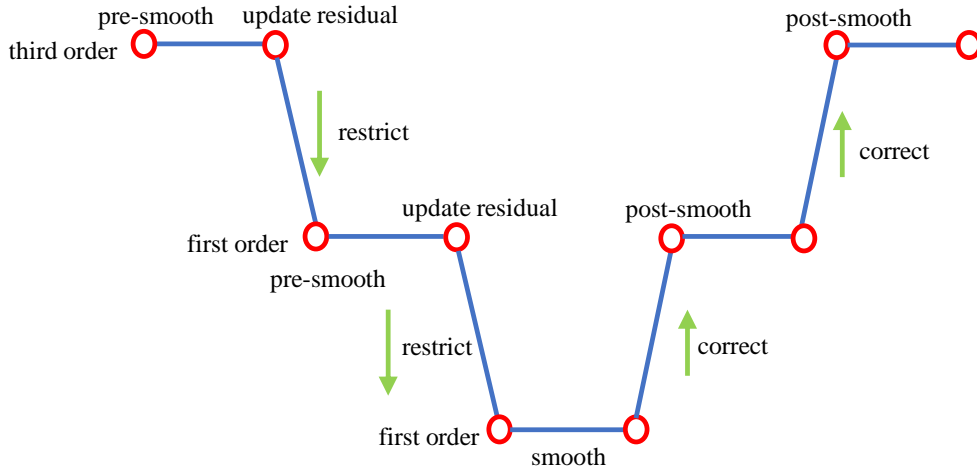


Figure 3: Hybrid method of geometric multigrid and p-multigrid.

4.3. Implicit time marching scheme on coarse mesh

In this section, we further implement the lower-upper symmetric Gauss-Seidel implicit relaxation on the coarse mesh. By comparing it with the explicit time marching scheme, the more efficient way for the time marching scheme of the geometric multigrid CGKS is explored. The implicit backward Euler method is used as the time discretization method, which is introduced as follows.

By using first-order backward Euler as time discretization method, the conservation laws become

$$|\Omega_i| \frac{\bar{\mathbf{U}}_i^{n+1} - \bar{\mathbf{U}}_i^n}{\Delta t} + \oint_{\partial\Omega} (\mathbf{F}_n^{n+1} - \mathbf{F}_n^n) ds = - \oint_{\partial\Omega} \mathbf{F}_n^n ds := \mathbf{R}_i^n \quad (29)$$

where $\mathbf{F}_n = \mathbf{F} \cdot \mathbf{n}$, \mathbf{n} is the outer unit normal direction for each interface, and \mathbf{F}_n^n is the explicit flux at t^n . Denote $\Delta \mathbf{U} = \bar{\mathbf{U}}^{n+1} - \bar{\mathbf{U}}^n$, the equation is simplified to be

$$|\Omega_i| \frac{\Delta \mathbf{U}_i}{\Delta t} + \oint_{\partial\Omega} (\mathbf{F}_n^{n+1} - \mathbf{F}_n^n) ds = \mathbf{R}_i^n \quad (30)$$

Linearize the term by first-order Taylor expansion

$$\mathbf{F}_n^{n+1} - \mathbf{F}_n^n \approx \left(\frac{\partial \mathbf{F}_n}{\partial \mathbf{U}} \right)^n (\mathbf{U}^{n+1} - \mathbf{U}^n) = \mathbf{A}^n \Delta \mathbf{U} \quad (31)$$

where $\mathbf{A} = \left(\frac{\partial \mathbf{F}_n}{\partial \mathbf{U}} \right) = \left(\frac{\partial (\mathbf{F} \cdot \mathbf{n})}{\partial \mathbf{U}} \right)$ is the Jacobian matrix of the normal flux. The Jacobian matrix of the first-order L-F flux is adopted, which is given by

$$\begin{aligned} (\mathbf{A} \Delta \mathbf{U})_{i,p} &= \mathbf{A}_{i,p}^+ \Delta \mathbf{U}_i + \mathbf{A}_{i,p}^- \Delta \mathbf{U}_{i,p} \\ \mathbf{A}^\pm &= \frac{1}{2} (\mathbf{A} \pm \lambda \mathbf{I}) \end{aligned} \quad (32)$$

where $\Delta \mathbf{U}_{i,p}$ is the increment of the conservative variable in the neighboring cell sharing the same interface Γ_{ip} . In computation, the modified spectral radius λ is adopted by

$$\lambda = |U_n| + c + 2\mu \frac{S}{|\Omega|} \quad (33)$$

Then we have

$$\oint_{\partial \Omega} \mathbf{A}^n \Delta \mathbf{U} \mathbf{d}s = \sum_{p=1}^{N_f} (\mathbf{A}_i^+ \Delta \mathbf{U}_i + \mathbf{A}_{i,p}^- \Delta \mathbf{U}_{i,p}) S_{i,p} \quad (34)$$

Substitute it into Eq. (30), we have

$$\Delta \mathbf{U}_i \left[\frac{|\Omega_i|}{\Delta t} + \frac{1}{2} \sum_{p=1}^{N_f} (\lambda S)_{i,p} \right] + \sum_{p=1}^{N_f} \mathbf{A}_{i,p}^- \Delta \mathbf{U}_{i,p} S_{i,p} = \mathbf{R}_{i,j}^n \quad (35)$$

where $\lambda_{i+1/2,j} = \text{Max}(\lambda_i, \lambda_{i,p})$.

The delta flux $\mathbf{A}_{i,p}^- \Delta \mathbf{U}_{i,p}$ is approximated as

$$\mathbf{A}_{i,p}^- \Delta \mathbf{U}_{i,p} \approx \Delta (\mathbf{F}_n)_{i,p}^- = \mathbf{F}_n^- (\mathbf{U}_{i,p}^n + \Delta \mathbf{U}_{i,p}) - \mathbf{F}_n^- (\mathbf{U}_{i,p}^n) \quad (36)$$

The local time step for each cell is used for both explicit and implicit time marching schemes.

Rewrite Eq. (35) as

$$\Delta \mathbf{U}_i \left[\frac{|\Omega_i|}{\Delta t_i} + \frac{1}{2} \sum_{p=1}^{N_f} (\lambda S)_{i,p} \right] + \sum_{p=1}^{N_f} [\mathbf{F}_n^- (\mathbf{U}_{i,p}^n + \Delta \mathbf{U}_{i,p}) - \mathbf{F}_n^- (\mathbf{U}_{i,p}^n)] = \mathbf{R}_{i,j}^n \quad (37)$$

where Δt_i is the local time step. Eq. (37) is the final form of the linear system. In this paper, a matrix-free point relaxation method is adopted to solve the linear system.

The convergence histories obtained from the numerical tests, such as subsonic flow around a sphere, transonic flow around a sphere and supersonic flow around a sphere, show that slight convergence speedup has been made by adopted LU-SGS method on coarse-level

mesh, as Fig. 4 shows. The improvement is insignificant and may destroy the performance of large-scale simulations.

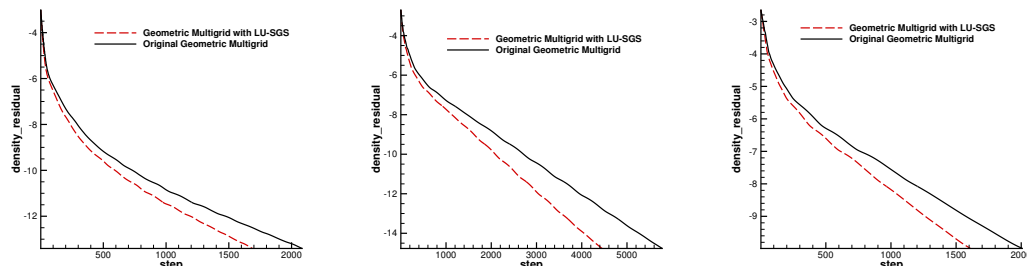


Figure 4: Convergence history of geometric multigrid with LU-SGS and original geometric multigrid. Left: Subsonic flow around a sphere, Mach number is 0.2535, Reynolds number is 118.0. Middle: Transonic flow around a sphere, Mach number is 0.95, Reynolds number is 300.0. Right: Supersonic flow around a sphere, Mach number is 2.0, Reynolds number is 300.0.

4.4. Parallel strategy of geometric multigrid

The convergence rate of implicit iterations like LU-SGS faces challenges when employing in large-scale simulations. Therefore, the scalability of implicit iterations for high-performance parallel computation is relatively poor. In this work, a parallel strategy of geometric multigrid is proposed, which has the advantage of having almost the same results between serial and parallel computations. As a result, it is convenient to apply multigrid algorithms to large-scale computations.

As mentioned before, for the finest mesh, this paper uses an explicit time-marching scheme and the parallel interfaces will not be merged when coarsening the mesh. These are the key reasons why the geometric multigrid CGKS has the advantage of having consistent results between serial and parallel computations. As Fig. 5 shows, when the fine mesh being coarsened to the coarse mesh, cell 1, cell 2, cell 3 and cell 4 of the fine mesh are merged into the new cell 1 of the coarse mesh. The parallel interfaces a and b of cell 2 and cell 4 of the fine mesh become the parallel interfaces a and b of cell 1 of the coarse mesh. This keeps the coarse meshes' parallel interface data structure the same as the one of fine meshes. As a result, this algorithm guarantees the non-docking faces will never appear at the parallel interfaces, preventing potential damage to the consistency of results in serial and parallel computation.

The convergence histories obtained from the numerical tests, such as subsonic flow around a sphere, transonic flow around a sphere and supersonic flow around a sphere, validate the consistency of results in serial and parallel computation, as Fig. 6 shows. Moreover, geometric multigrid CGKS with LU-SGS can't be extended to large-scale computation, because as Fig. 7 shows, its convergence rate decreases with the CPU cores increase. Therefore, the explicit time marching scheme on each level mesh with the local time stepping technique is suggested for the proposed method.

The whole geometric multigrid p-multigrid CGKS algorithm flowchart is shown as Fig. 8.

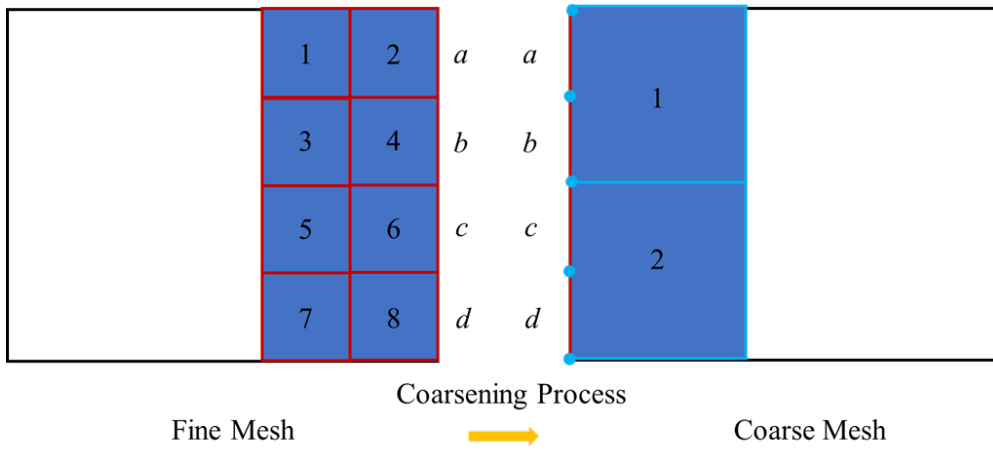


Figure 5: Hybrid method of geometric multigrid and p-multigrid.

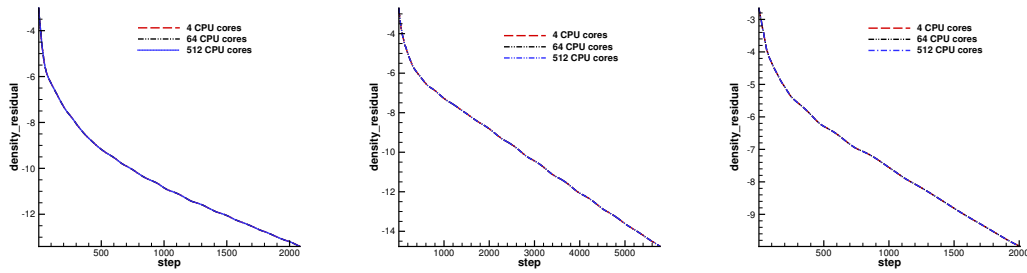


Figure 6: Convergence history under the computation condition of 4, 32, 512 CPU cores. Left: Subsonic flow around a sphere. Mid: Transonic flow around a sphere. Right: Supersonic flow around a sphere.

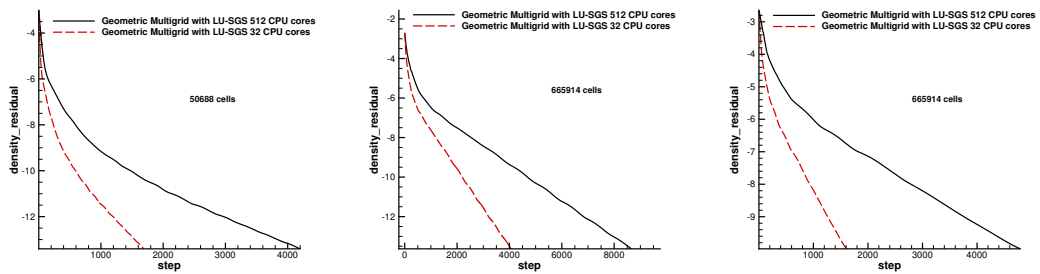


Figure 7: Convergence history of geometric multigrid CGKS with LU-SGS under the computation condition of 32 and 512 CPU cores. Left: Subsonic flow around a sphere. Mid: Transonic flow around a sphere. Right: Supersonic flow around a sphere.

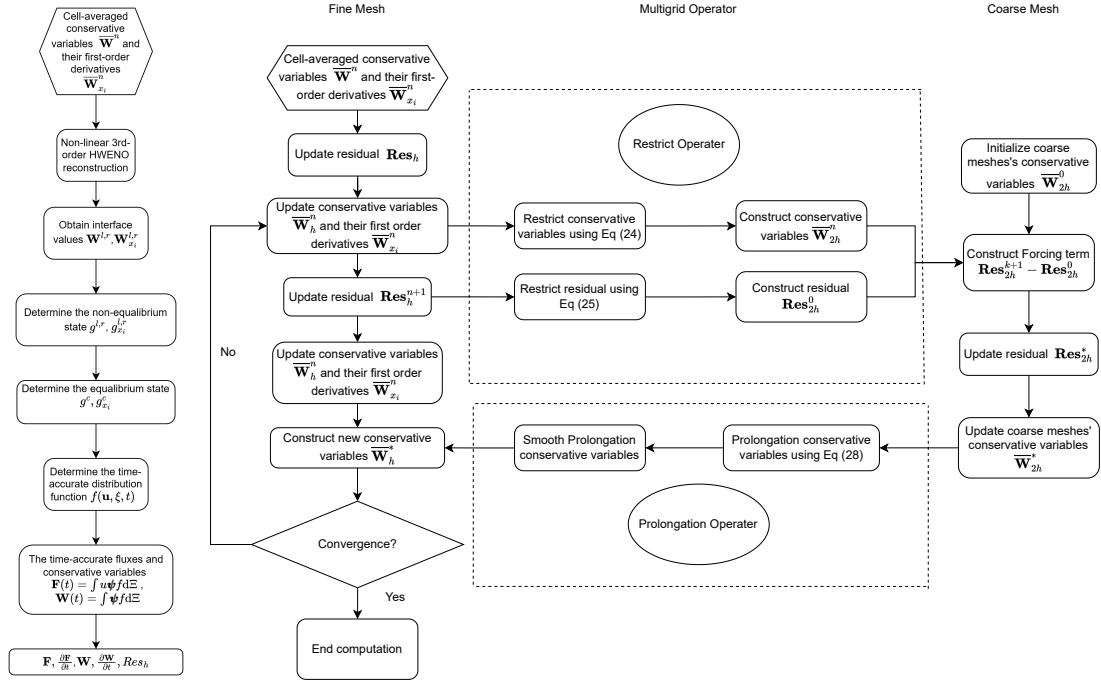


Figure 8: Geometric multigrid p-multigrid CGKS algorithm flowchart. Left: Residual updating procedure of Explicit third-order CGKS. Right: Multigrid procedure with pre-smooth number is 1 and post smooth number is 0 if not specified.

5. Numerical examples

In this section, numerical tests are presented to validate the proposed scheme. All the simulations are performed on 3-D hybrid unstructured mesh. The simulations are conducted by our in-house C++ solver, where MPI is used for parallel computation, and METIS is used for mesh partitioning.

5.1. Flow around a sphere

(a) subsonic viscous flow around a sphere

A subsonic flow around a sphere is simulated in this case. The Mach number is set to be 0.2535 and the Reynolds number is set to be 118.0. The first mesh off the wall has the size $h = 4.5 \times 10^{-2}D$, and the total cell number is 50688. A three-layer “V” cycle p-multigrid geometric multigrid is used to solve the case. The finest mesh is shown in Fig. 9. The coarse meshes at the second level and the third level are shown in Fig. 10 and Fig. 11.

The residuals can be reduced to below 10^{-10} for both explicit CGKS and geometric-multigrid CGKS. The iteration number of the geometric-multigrid CGKS is about 1/14 of the number of iteration steps of the explicit CGKS at a residual level of 10^{-10} , as shown in Fig. 12. The CPU time speedup for geometric-multigrid CGKS is about 6.67. The comparison result of convergence history between geometric-multigrid CGKS and p-multigrid CGKS [21] shown in Fig. 12 indicates that the convergence rate of the geometric-multigrid CGKS is 5 times faster than that of p-multigrid CGKS at the residual level 10^{-8} . The Mach number contour

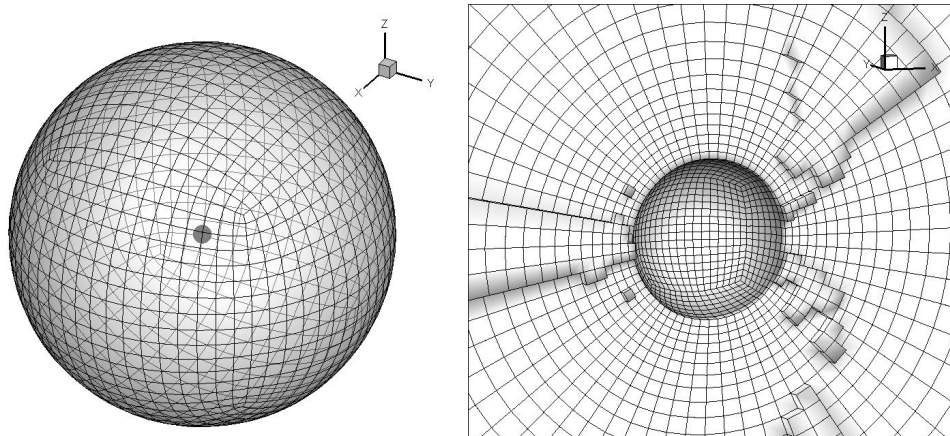


Figure 9: Subsonic flow around a sphere. Mesh sample.

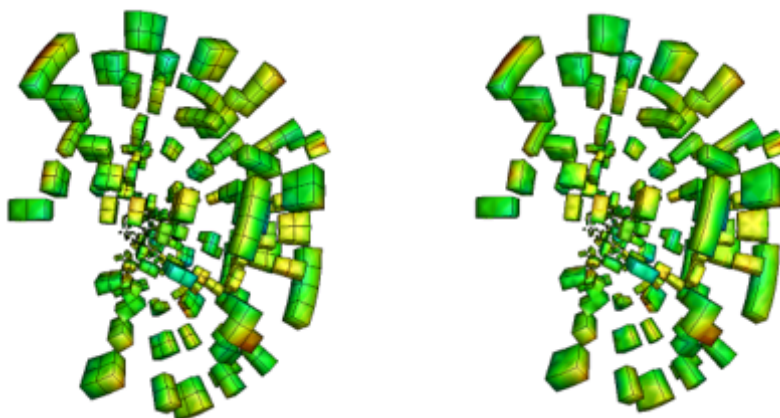


Figure 10: Subsonic flow around a sphere. The second layer coarse mesh.

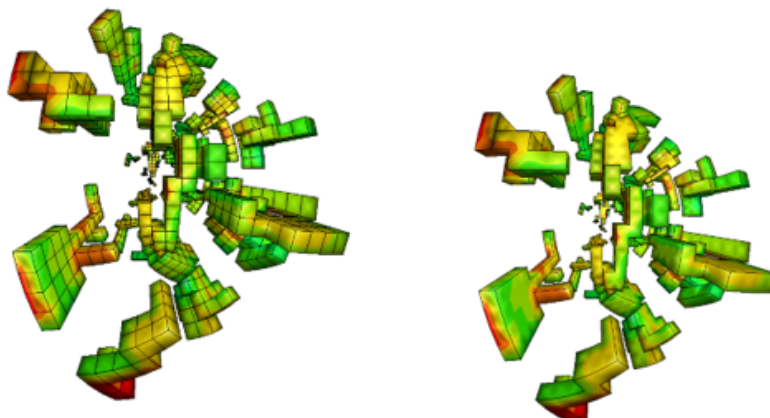


Figure 11: Subsonic flow around a sphere. The third layer coarse mesh.

and streamline are also presented in Fig. 13 to show the high resolution of the CGKS. Quantitative results are given in Table 1, including the drag coefficient C_d , the separation angle θ , and the closed wake length L , as defined in [22].

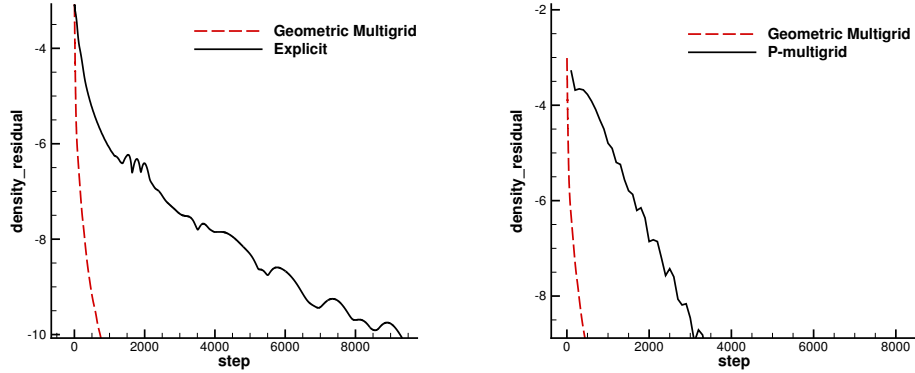


Figure 12: Residual compare. Left: Geometric-multigrid CGKS compared with explicit CGKS. Right: Geometric-multigrid CGKS compared with p-multigrid CGKS

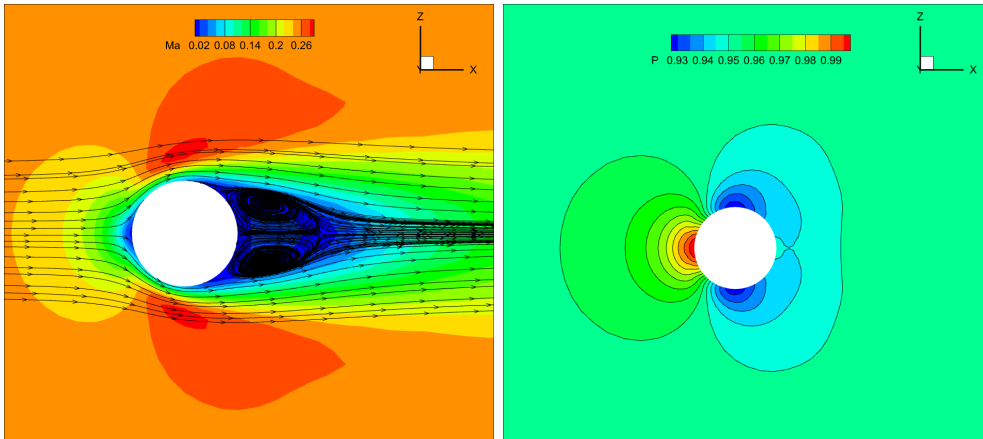


Figure 13: Subsonic flow around a sphere. Left: Mach contour and streamlines obtained by the geometric-multigrid CGKS. Right: Pressure contour obtained by geometric-multigrid CGKS

(b) *transonic viscous flow around a sphere*

A transonic viscous flow around a sphere is simulated to show the performance of the geometric multigrid CGKS for transonic viscous flow. The Mach number is set to be 0.95 and Reynolds number is set to be 300.0. A three layer "V" cycle p-multigrid geometric multigrid is used to solve the case. The mesh used in this case is the same as the supersonic case. Fig. 14 shows that the iteration steps of the geometric-multigrid CGKS is about 1/25 of the iteration steps of the explicit CGKS. The CPU time costed by explicit CGKS is 9.54 times more than geometric-multigrid CGKS. Comparison has also been made between geometric-multigrid CGKS and p-multigrid CGKS. The result in Fig. 14 shows geometric-multigrid

Scheme	Mesh number	Cd	θ	L	Cl
Experiment [44]	–	1.0	151	1.07	–
Third-order DDG [12]	160,868	1.016	123.7	0.96	–
Fourth-order VFV [46]	458,915	1.014	–	–	2.0e-5
Current	50688	1.021	126.6	0.94	2.33e-5

Table 1: Quantitative comparisons among different compact schemes for the subsonic flow around a sphere.

CGKS has a faster convergence rate. The numerical results of the Mach number contour and streamline around a sphere are shown in Fig. 15, which indicates the high resolution of CGKS.

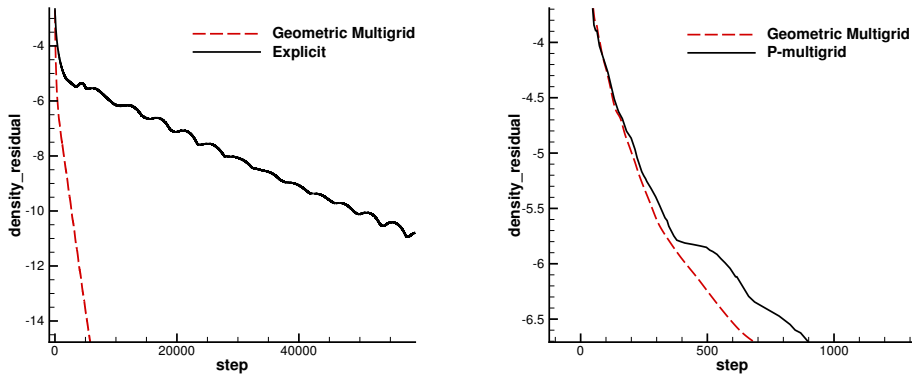


Figure 14: Residual compare. Left: Geometric CGKS compared with explicit CGKS. Right: Geometric Multigrid CGKS compared with p-multigrid CGKS.

Scheme	Mesh Number	Cd	θ	L
WENO6 [32]	909,072	0.968	111.5	3.48
Current	665,914	0.963	110.0	3.44

Table 2: Quantitative comparisons between the current scheme and the reference solution for the transonic flow around a sphere.

(c) *supersonic viscous flow around a sphere*

To verify that geometric-multigrid CGKS can also have good performance in the supersonic flow region, a supersonic flow around a sphere is simulated. The Mach number is set to be 1.2 and the Reynolds number is set to be 300. A three layer "V" cycle p-multigrid geometric multigrid is used to solve the case. The mesh used in this case is shown in Fig. 16. The upstream length is 5 and the downstream length is 40. The first layer mesh at the wall has a thickness $2.3 \times 10^{-2}D$. The iteration steps of the geometric-multigrid CGKS is about 1/8 of the iteration steps of the explicit CGKS. Also, compared with explicit CGKS at the residual level 10^{-8} , 2.67 times speedup of CPU time can be achieved, as Fig. 17 shows. The

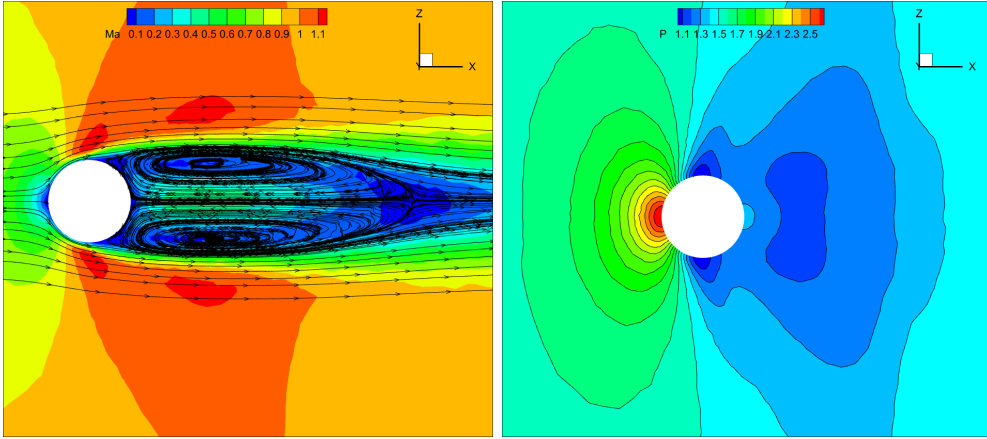


Figure 15: Transonic flow around a sphere. Left: Mach number contour with streamline through the sphere. Right: Pressure contour.

result of Mach number with streamline around the sphere is also shown in Fig. 17, which indicates the high resolution of CGKS. Quantitative results are listed in Table 3, which has good agreement with those given by Ref.[32] .

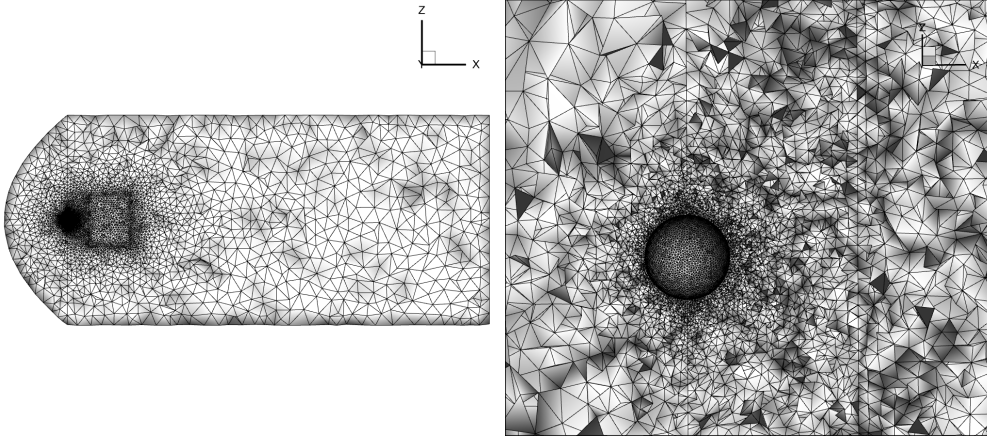


Figure 16: Supersonic flow around a sphere. Mesh sample. Left: Global mesh. Right: Local mesh

5.2. M6-wing

Transonic flow around an ONERA M6 [13] wing is a standard engineering case to verify the acceleration techniques used in CFD [52]. The flow structure of it is complicated due to the interaction of shock and wall boundary. What is more, three-dimensional mixed unstructured mesh is also a challenge to high-order schemes with acceleration techniques. Thus, it is an appropriate test case to verify the efficiency and robustness of the geometric-multigrid CGKS. The farfield Mach number is set to be 0.8395 and the angle of attack is set to be 3.06° . The adiabatic slip wall boundary is used on the surface of the ONERA M6 wing and the subsonic inflow boundary is set according to the local Riemann invariants. A

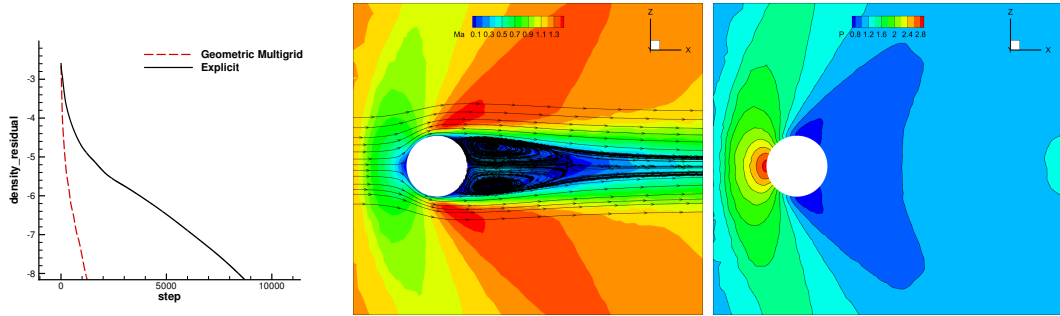


Figure 17: Numerical result of supersonic flow around a sphere. Left: Convergence history of geometric-multigrid CGKS and explicit CGKS. Mid: Mach number contour with streamline around a sphere. Right: Pressure contour.

Scheme	Mesh Number	Cd	θ	L	Shock stand-off
WENO6 [32]	909,072	1.281	126.9	1.61	0.69
Current	665,914	1.296	126.3	1.60	0.72

Table 3: Quantitative comparisons between the current scheme and the reference solution for the supersonic flow around a sphere.

three layer "V" cycle p-multigrid geometric multigrid is used to solve the case. A hybrid unstructured mesh with a near-wall size $h \approx 2e^{-3}$ is used in the computation, as shown in Fig. 18. The iteration steps of the geometric-multigrid CGKS is about 1/20 of the iteration steps of the explicit CGKS. Also, compared with explicit CGKS a 6.70 times speedup of CPU time is achieved, as shown in Fig. 18. The pressure distribution on the wall surface and the Mach number slices at different wing sections are shown in Fig. 19. The pressure and Mach number contour in Fig. 19 indicates that the p-multigrid geometric multigrid CGKS has captured the shock accurately. The quantitative comparisons on the pressure distributions at the semi-span locations $Y/B = 0.20, 0.44, 0.65, 0.80, 0.90$ and 0.95 of the wing are given in Fig. 20. The numerical results quantitatively agree well with the experimental data.

5.3. Subsonic flow around a NACA0012 airfoil

(a) viscous flow with zero angle of attack

In this section, viscous flow around a NACA0012 airfoil is simulated. The incoming Mach number is set to be 0.5 and the incoming Reynolds number is set to be 5000 based on the chord length $L=1$. The subsonic farfield is calculated by Riemann invariants and the solid wall of the airfoil is set to be a adiabatic non-slip wall. Total 6538×2 hybrid prismatic cells are used in a cuboid domain $[-15, 15] \times [15, 15] \times [0, 0.1]$. The hybrid unstructured mesh is shown in Fig. 21. A three layer "V" cycle p-multigrid geometric multigrid is used to solve the case. From the residual result shown in Fig. 22, the iteration steps of the geometric-multigrid CGKS is about 1/12 of the iteration steps of the explicit CGKS. Also, a 3.89 times speedup in CPU time is achieved compared with explicit CGKS. The Mach number contour is shown in Fig. 22. Quantitative result including the surface pressure coefficient is extracted and plotted in Fig. 23, which highly agrees with the Ref [4].

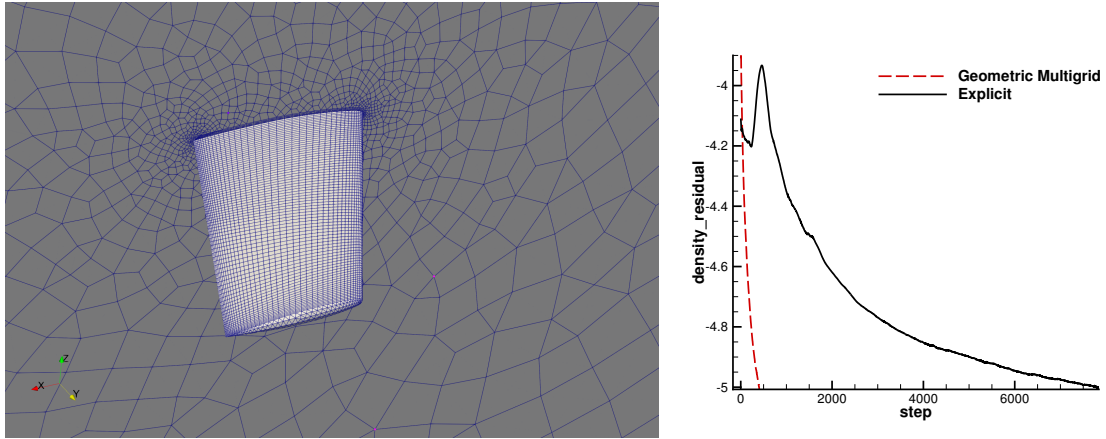


Figure 18: Transonic flow around a M6 wing. Left: Hybrid unstructured mesh. Right: Convergence history.

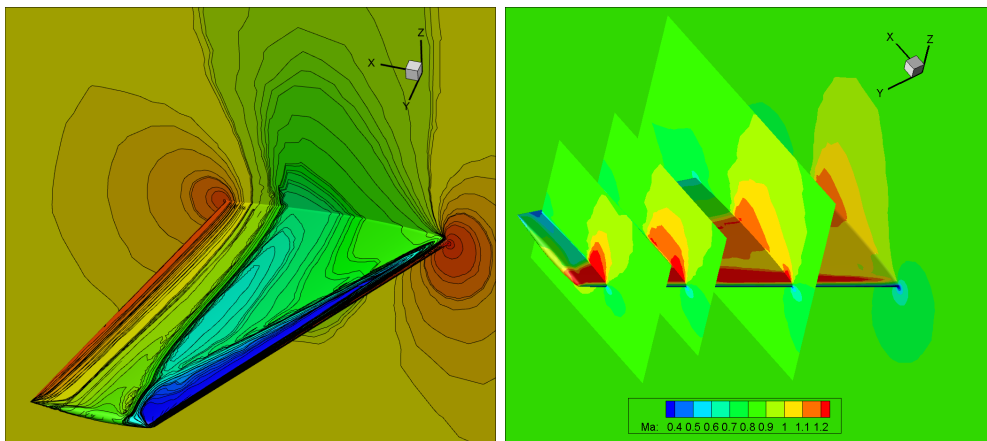


Figure 19: Transonic flow around a M6 wing. Left: Pressure contour. Right: Mach number contour.

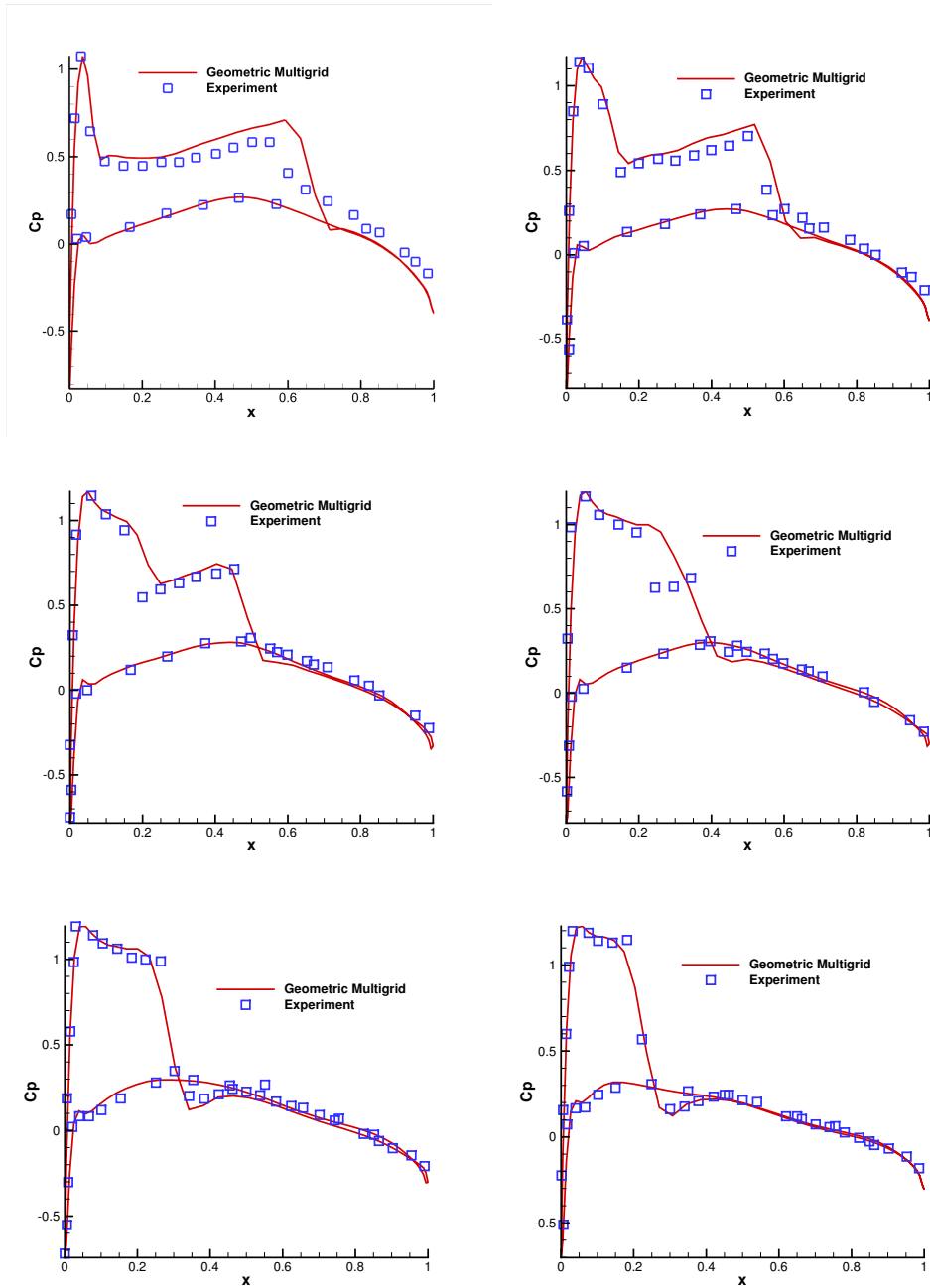


Figure 20: Transonic flow around a M6 wing. C_p distribution

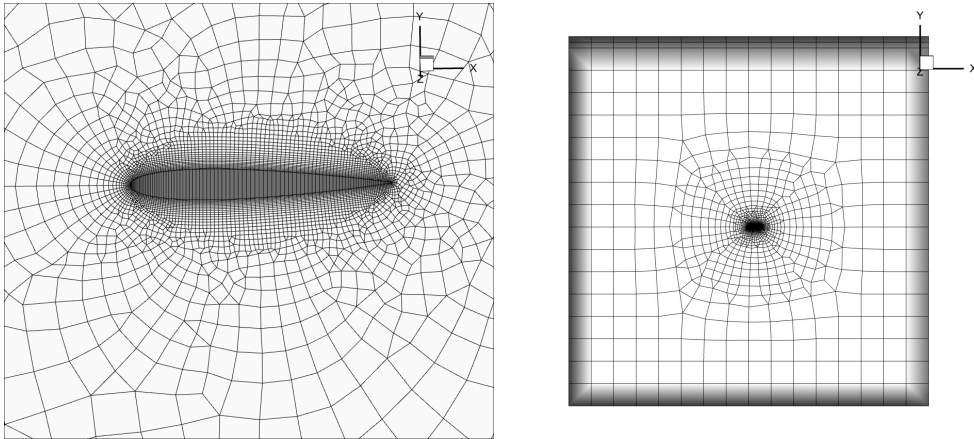


Figure 21: NACA0012 airfoil Mesh.

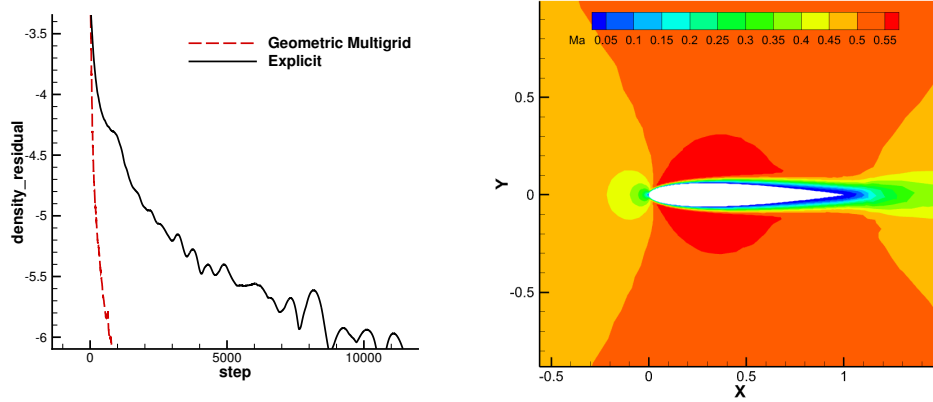


Figure 22: Subsonic flow around a NACA0012 airfoil. Left: convergence history. Right: Mach number contour.

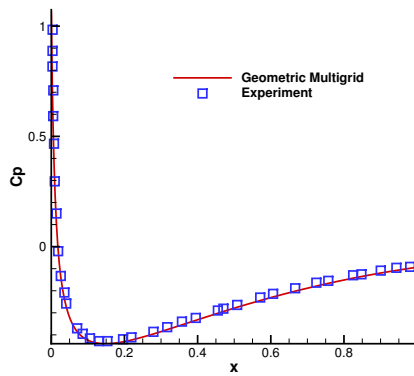


Figure 23: Subsonic flow around a NACA0012 airfoil. Surface pressure coefficient distribution.

(b) *viscous flow with an angle of attack*

In this case, except the angle of attack is set to be 8° , flow conditions are the same with the case of zero angle. A three layer "V" cycle p-multigrid geometric multigrid is used to solve the case. From the convergence history shown in Fig. 24, the iteration steps of the geometric-multigrid CGKS is about 1/11 of the iteration steps of the explicit CGKS. Also, a 3.8 times speedup in CPU time is achieved compared with explicit CGKS. The Mach number contour with streamline through the airfoil and the pressure contour are shown in Fig. 24.

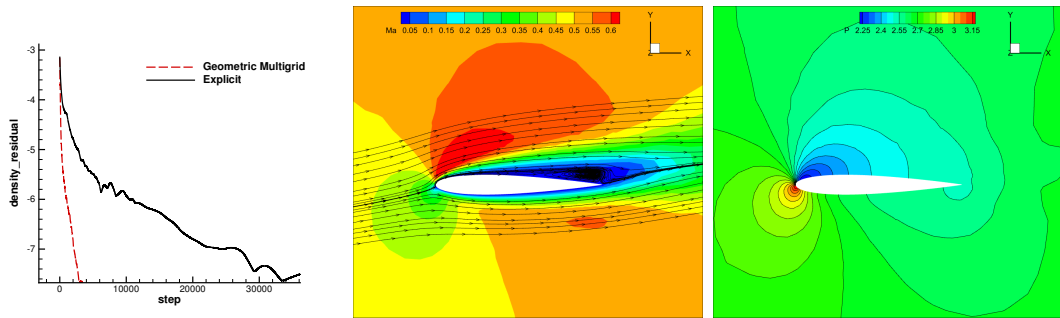


Figure 24: Subsonic flow around a NACA0012 airfoil with an angle of attack. Left: Convergence history. Mid: Mach number contour. Right: Pressure contour.

5.4. *Transonic flow around dual NACA0012 airfoils*

To further verify that the geometric-multigrid CGKS has a good performance both on complex geometry and discontinuity, transonic flow around dual NACA0012 airfoils is simulated. The head of the first airfoil is located at $(0, 0)$ and the second one is located at $(0.5, 0.5)$. Both airfoils are put in parallel with the x-axis. The incoming Mach number is set to be 0.8 with an angle of attack $AOA = 10^\circ$ and the Reynolds number is set to be 500 based on the chord length $L = 1$. The mesh consists 28678 mixed elements. The near wall size of the mesh is set to be $h = 2 \times 10^{-3}$, which indicates that the grid Reynolds number is 2.5×10^5 . The farfield boundary condition is set to be subsonic inflow using Riemann invariants and the wall is set to be a non-slip adiabatic wall. The mesh is presented in Fig. 25. In this case, the iteration steps of the geometric-multigrid CGKS is about 1/24 of the iteration steps of the explicit CGKS. Also, a 8 times speedup of CPU time is achieved compared with explicit CGKS shown in Fig. 26. The Mach number distribution and the pressure distribution are shown in Fig. 27. The oblique shock wave can be observed at the front of the top airfoil. The surface pressure coefficient is also extracted and compared with the reference data [18], as shown in Fig. 28. The result obtained by geometric-multigrid CGKS agrees well with the experimental data.

6. **Conclusions**

In this study, we integrate a geometric multigrid approach with the compact gas-kinetic scheme (CGKS) to enhance computational efficiency. A rapid coarse mesh generation technique minimizes the time typically required for mesh coarsening. We employ a three-layer

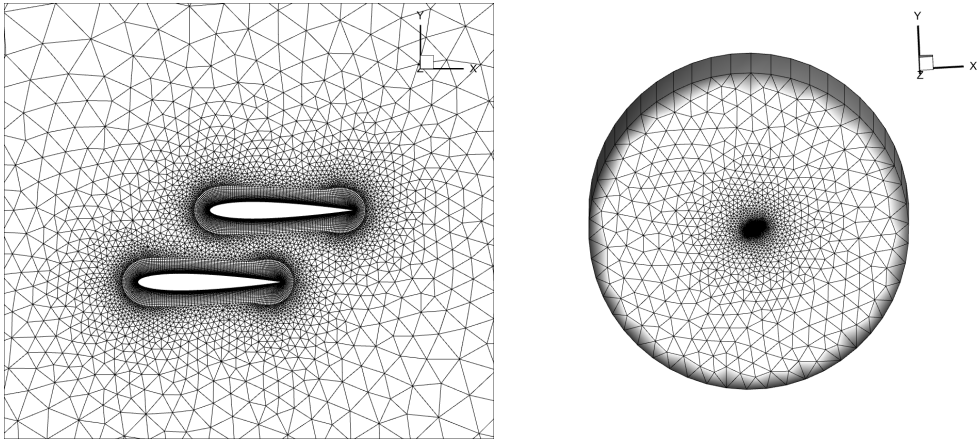


Figure 25: Transonic flow around dual NACA0012 airfoils. Mesh.

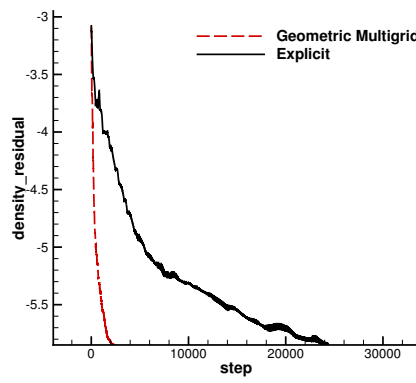


Figure 26: Transonic flow around dual NACA0012 airfoils. Convergence history.

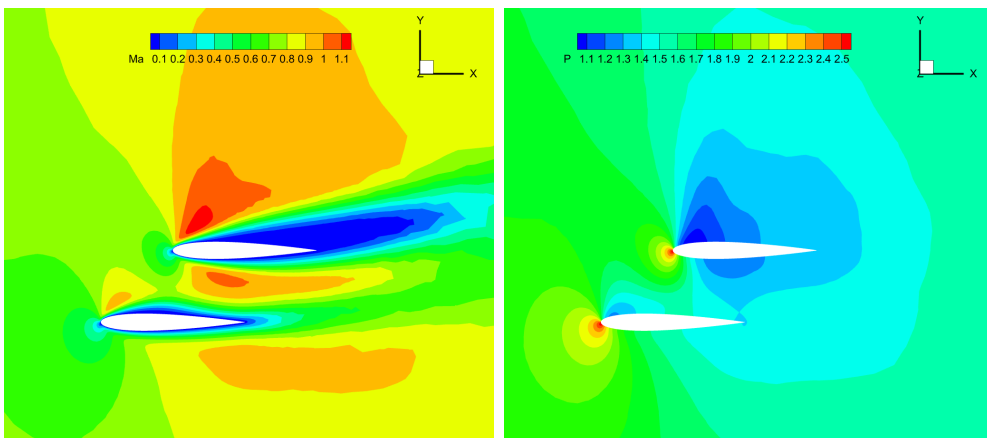


Figure 27: Transonic flow around dual NACA0012 airfoils. Left: Mach number distribution. Right: Pressure distribution.

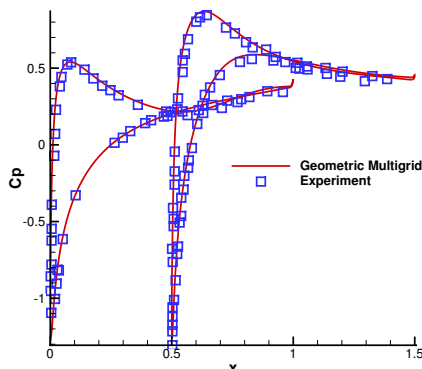


Figure 28: Transonic flow around dual NACA0012 airfoils. Surface pressure coefficient distribution.

V-cycle algorithm to hasten the scheme’s convergence, using a single-step third-order CGKS for the finest mesh, while a first-order kinetic flux vector splitting scheme with local time stepping addresses low-frequency errors on coarser levels. The parallel communication strategy for the coarse mesh is both straightforward and time-efficient. We demonstrate the method’s performance on 3-D hybrid unstructured meshes, achieving a three to tenfold reduction in CPU time compared to the conventional explicit CGKS. Notably, the method preserves result consistency across serial and parallel computations, suggesting its suitability for large-scale applications, including multi-GPU acceleration. Our analysis indicates that the geometric multigrid method offers greater acceleration in transonic flows compared to supersonic ones, with quantitative results closely matching those from explicit methods. Future work will explore incorporating implicit schemes like the GMRES method into the geometric multigrid framework to further elevate the convergence rate.

Acknowledgments

The current research is supported by National Science Foundation of China (12172316, 12302378, 92371201, 92371107), Hong Kong Research Grant Council (16208021,16301222).

References

References

- [1] Remi Abgrall and Mario Ricchiuto. High-order methods for CFD. *Encyclopedia of Computational Mechanics Second Edition*, pages 1–54, 2018.
- [2] Antonis F. Antoniadis, Panagiotis Tsoutsanis, and Dimitris Drikakis. Assessment of high-order finite volume methods on unstructured meshes for RANS solutions of aeronautical configurations. *Computers & Fluids*, 146:86 – 104, 2017.
- [3] F. Bassi, A. Ghidoni, S. Rebay, and P. Tesini. High-order accurate p-multigrid discontinuous Galerkin solution of the Euler equations. *International Journal for Numerical Methods in Fluids*, 60(8):847–865, 2009.

- [4] F. Bassi and S. Rebay. A high-order accurate discontinuous finite element method for the numerical solution of the compressible Navier-Stokes equations. *Journal of Computational Physics*, 131(2):267–279, 1997.
- [5] Prabhu Lal Bhatnagar, Eugene P Gross, and Max Krook. A model for collision processes in gases. I. Small amplitude processes in charged and neutral one-component systems. *Physical Review*, 94(3):511, 1954.
- [6] Muhammad Mubashir Bhatti, M Marin, Ahmed Zeeshan, and Sara I Abdelsalam. Recent trends in computational fluid dynamics. *Frontiers in Physics*, 8:593111, 2020.
- [7] J Blazek, C-C Rossow, N Kroll, and RC Swanson. A comparison of several implicit residual smoothing methods in combination with multigrid. In *Thirteenth International Conference on Numerical Methods in Fluid Dynamics: Proceedings of the Conference Held at the Consiglio Nazionale delle Ricerche Rome, Italy, 6–10 July 1992*, pages 386–390. Springer, 2005.
- [8] William L Briggs, Van Emden Henson, and Steve F McCormick. *A multigrid tutorial*. SIAM, 2000.
- [9] Clément Cances, Thomas O Gallouët, and Gabriele Todeschi. A variational finite volume scheme for wasserstein gradient flows. *Numerische Mathematik*, 146:437–480, 2020.
- [10] Carlo Cercignani and Carlo Cercignani. *The Boltzmann equation*. Springer, 1988.
- [11] Sydney Chapman and Thomas George Cowling. *The mathematical theory of non-uniform gases: an account of the kinetic theory of viscosity, thermal conduction and diffusion in gases*. Cambridge University Press, 1970.
- [12] Jian Cheng, Xiaodong Liu, Tiegang Liu, and Hong Luo. A parallel, high-order direct discontinuous Galerkin method for the Navier-Stokes equations on 3D hybrid grids. *Communications in Computational Physics*, 21(5):1231–1257, 2017.
- [13] Bernhard Eisfeld. ONERA M6 wing. In *FLOMANIA—A European Initiative on Flow Physics Modelling: Results of the European-Union funded project, 2002–2004*, pages 219–224. Springer, 2006.
- [14] E Ferrer, G Rubio, G Ntoukas, W Laskowski, OA Mariño, S Colombo, A Mateo-Gabín, H Marbona, F Manrique de Lara, D Huelgo, et al. : A high-order discontinuous Galerkin solver for flow simulations and multi-physics applications. *Computer Physics Communications*, 287:108700, 2023.
- [15] Zhen Gao, Wai Sun Don, and Zhiqiu Li. High order weighted essentially non-oscillation schemes for two-dimensional detonation wave simulations. *Journal of Scientific Computing*, 53:80–101, 2012.
- [16] T. Haga, H. Gao, and Z. J. Wang. A high-order unifying discontinuous formulation for the Navier-Stokes equations on 3D mixed grids. *Mathematical Modelling of Natural Phenomena*, 6(3):28–56, 2011. Section: 28.
- [17] H.T. Huynh, Z.J. Wang, and P.E. Vincent. High-order methods for computational fluid dynamics: A brief review of compact differential formulations on unstructured grids. *Computers & Fluids*, 98:209–220, 2014. 12th USNCCM mini-symposium of High-Order Methods for Computational Fluid Dynamics - A special issue dedicated to the 80th birthday of Professor Antony Jameson.
- [18] P. Jawahar and Hemant Kamath. A high-resolution procedure for Euler and Navier-Stokes computations on unstructured grids. *Journal of Computational Physics*, 164(1):165–203, 2000.
- [19] Xing Ji, Liang Pan, Wei Shyy, and Kun Xu. A compact fourth-order gas-kinetic scheme for the Euler and Navier-Stokes equations. *Journal of Computational Physics*, 372:446 – 472, 2018.
- [20] Xing Ji, Wei Shyy, and Kun Xu. A gradient compression-based compact high-order gas-kinetic scheme on 3d hybrid unstructured meshes. *International Journal of Computational Fluid Dynamics*, 35(7):485–509, 2021.
- [21] Xing Ji, Wei Shyy, and Kun Xu. A p-multigrid compact gas-kinetic scheme for steady-state acceleration. *Computers & Fluids*, 241:105489, 2022.
- [22] Xing Ji, Fengxiang Zhao, Wei Shyy, and Kun Xu. Compact high-order gas-kinetic scheme for three-dimensional flow simulations. *AIAA Journal*, 0(0):1–18, 0.
- [23] Xing Ji, Fengxiang Zhao, Wei Shyy, and Kun Xu. A HWENO reconstruction based high-order compact gas-kinetic scheme on unstructured mesh. *Journal of Computational Physics*, page 109367, 2020.
- [24] Xing Ji, Fengxiang Zhao, Wei Shyy, and Kun Xu. Two-step multi-resolution reconstruction-based compact gas-kinetic scheme on tetrahedral mesh. *Journal of Computational Physics*, 497:112590, 2024.

- [25] Ji Li, Chengwen Zhong, Yong Wang, and Congshan Zhuo. Implementation of dual time-stepping strategy of the gas-kinetic scheme for unsteady flow simulations. *Physical Review E*, 95:053307, 2017.
- [26] Jiayin Li, Chi-Wang Shu, and Jianxian Qiu. Multi-resolution hweno schemes for hyperbolic conservation laws. *Journal of Computational Physics*, 446:110653, 2021.
- [27] Jiequan Li and Zhifang Du. A two-stage fourth order time-accurate discretization for Lax–Wendroff type flow solvers I. hyperbolic conservation laws. *SIAM Journal on Scientific Computing*, 38(5):A3046–A3069, 2016.
- [28] Xinliang Li, Dexun Fu, and Yanwen Ma. Direct numerical simulation of hypersonic boundary layer transition over a blunt cone with a small angle of attack. *Physics of Fluids*, 22(2), 2010.
- [29] C. Liang, R. Kannan, and Z.J. Wang. A p-multigrid spectral difference method with explicit and implicit smoothers on unstructured triangular grids. *Computers & Fluids*, 38(2):254–265, 2009.
- [30] Hong Luo, Joseph D. Baum, and Rainald Löhner. A p-multigrid discontinuous Galerkin method for the Euler equations on unstructured grids. *Journal of Computational Physics*, 211(2):767–783, 2006.
- [31] Dimitri J Mavriplis and Antony Jameson. Multigrid solution of the Navier-Stokes equations on triangular meshes. *AIAA journal*, 28(8):1415–1425, 1990.
- [32] T. Nagata, T. Nonomura, S. Takahashi, Y. Mizuno, and K. Fukuda. Investigation on subsonic to supersonic flow around a sphere at low Reynolds number of between 50 and 300 by direct numerical simulation. *Physics of Fluids*, 28(5):056101, 2016.
- [33] Amir Nejat and Carl Ollivier-Gooch. A high-order accurate unstructured finite volume Newton-Krylov algorithm for inviscid compressible flows. *Journal of Computational Physics*, 227(4):2582–2609, 2008.
- [34] Liang Pan and Kun Xu. High-order gas-kinetic scheme with three-dimensional WENO reconstruction for the Euler and Navier-Stokes solutions. *Computers & Fluids*, 198:104401, 2020.
- [35] John W. Pearson and Jennifer Pestana. Preconditioners for Krylov subspace methods: An overview. *GAMM-Mitteilungen*, 43(4):e202000015, 2020.
- [36] Christopher M Romick and Tariq D Aslam. High-order shock-fitted detonation propagation in high explosives. *Journal of Computational Physics*, 332:210–235, 2017.
- [37] Einar M. Rønquist and Anthony T. Patera. Spectral element multigrid. I. Formulation and numerical results. *Journal of Scientific Computing*, 2(4):389–406, 1987.
- [38] Youcef Saad and Martin H. Schultz. GMRES: A generalized minimal residual algorithm for solving nonsymmetric linear systems. *SIAM Journal on Scientific and Statistical Computing*, 7(3):856–869, 1986.
- [39] Eiji Shima, Keiichi Kitamura, and Takanori Haga. Green–gauss/weighted-least-squares hybrid gradient reconstruction for arbitrary polyhedra unstructured grids. *AIAA journal*, 51(11):2740–2747, 2013.
- [40] Chi-Wang Shu. High-order finite difference and finite volume WENO schemes and discontinuous Galerkin methods for CFD. *International Journal of Computational Fluid Dynamics*, 17(2):107–118, 2003.
- [41] Chi-Wang Shu. High order WENO and DG methods for time-dependent convection-dominated PDEs: A brief survey of several recent developments. *Journal of Computational Physics*, 316:598 – 613, 2016.
- [42] Klaus Stüben. A review of algebraic multigrid. *Numerical Analysis: Historical Developments in the 20th Century*, pages 331–359, 2001.
- [43] Shuang Tan and Qibing Li. Time-implicit gas-kinetic scheme. *Computers & Fluids*, 144:44–59, 2017.
- [44] Sadatoshi Taneda. Experimental investigation of the wakes behind cylinders and plates at low Reynolds numbers. *Journal of the Physical Society of Japan*, 11(3):302–307, 1956.
- [45] Gang Wang, Yuewen Jiang, and Zhengyin Ye. An improved LU-SGS implicit scheme for high Reynolds number flow computations on hybrid unstructured mesh. *Chinese Journal of Aeronautics*, 25(1):33–41, 2012.
- [46] Qian Wang. *Compact High-Order Finite Volume Method on Unstructured Grids*. PhD thesis, Tsinghua University, 6 2017.
- [47] ZJ Wang, Y Li, F Jia, GM Laskowski, J Kopriva, U Paliath, and R Bhaskaran. Towards industrial large eddy simulation using the FR/CPR method. *Computers & Fluids*, 156:579–589, 2017.
- [48] Pieter Wesseling and Cornelis W Oosterlee. Geometric multigrid with applications to computational

- fluid dynamics. *Journal of computational and applied mathematics*, 128(1-2):311–334, 2001.
- [49] Roman Wienands, Cornelis W Oosterlee, and Takumi Washio. Fourier analysis of GMRES (m) preconditioned by multigrid. *SIAM Journal on Scientific Computing*, 22(2):582–603, 2000.
- [50] Kun Xu. *Direct Modeling for Computational Fluid Dynamics: Construction and Application of Unified Gas-Kinetic Schemes*, chapter 2. World Scientific, 2014.
- [51] Xiaoquan Yang, Jian Cheng, Hong Luo, and Qijun Zhao. Robust implicit direct discontinuous Galerkin method for simulating the compressible turbulent flows. *AIAA Journal*, 57(3):1113–1132, 2019.
- [52] Yaqing Yang, Liang Pan, and Kun Xu. Implicit high-order gas-kinetic schemes for compressible flows on three-dimensional unstructured meshes. *arXiv preprint arXiv:2304.09485*, 2023.
- [53] Jian Zhang, Liang Deng, Ruitian Li, Ming Li, Jie Liu, and Zhe Dai. Achieving high performance and portable parallel GMRES algorithm for compressible flow simulations on unstructured grids. *J. Supercomput.*, 79(17):20116–20140, 2023.
- [54] Laiping Zhang, Zhong Zhao, Xinghua Chang, and Xin He. A 3D hybrid grid generation technique and a multigrid/parallel algorithm based on anisotropic agglomeration approach. *Chinese Journal of Aeronautics*, 26(1):47–62, 2013.
- [55] Yue Zhang, Xing Ji, and Kun Xu. A high-order compact gas-kinetic scheme in a rotating coordinate frame and on sliding mesh. *International Journal of Computational Fluid Dynamics*, 0(0):1–20, 2023.
- [56] Fengxiang Zhao, Xing Ji, Wei Shyy, and Kun Xu. Compact higher-order gas-kinetic schemes with spectral-like resolution for compressible flow simulations. *Advances in Aerodynamics*, 1(1):13, 2019.
- [57] Fengxiang Zhao, Xing Ji, Wei Shyy, and Kun Xu. An acoustic and shock wave capturing compact high-order gas-kinetic scheme with spectral-like resolution. *International Journal of Computational Fluid Dynamics*, pages 1–26, 2020.
- [58] Fengxiang Zhao, Xing Ji, Wei Shyy, and Kun Xu. High-order compact gas-kinetic schemes for three-dimensional flow simulations on tetrahedral mesh. *Advances in Aerodynamics*, 5(1):1–28, 2023.
- [59] Jun Zhu and Chi-Wang Shu. A new type of third-order finite volume multi-resolution WENO schemes on tetrahedral meshes. *Journal of Computational Physics*, 406:109212, 2020.
- [60] Yajun Zhu, Chengwen Zhong, and Kun Xu. Implicit unified gas-kinetic scheme for steady state solutions in all flow regimes. *Journal of Computational Physics*, 315:16–38, 2016.